



# 3D-3D porous $\text{Bi}_2\text{WO}_6$ /graphene hydrogel composite with excellent synergistic effect of adsorption-enrichment and photocatalytic degradation

Jinjin Yang <sup>a</sup>, Daimei Chen <sup>b,\*</sup>, Yi Zhu <sup>a</sup>, Yuanming Zhang <sup>a,\*</sup>, Yongfa Zhu <sup>c,\*</sup>

<sup>a</sup> Department of Chemistry, Jinan University, Guangzhou 510632, China

<sup>b</sup> National Laboratory of Mineral Materials, School of Materials Sciences and Technology, China University of Geosciences, Beijing 100083, China

<sup>c</sup> Department of Chemistry, Tsinghua University, Beijing 100084, China



## ARTICLE INFO

### Article history:

Received 4 October 2016

Received in revised form 8 December 2016

Accepted 11 December 2016

Available online 12 December 2016

### Keywords:

$\text{Bi}_2\text{WO}_6$

Graphene hydrogel

3D-3D structure

Synergy

Photocatalysis

## ABSTRACT

A novel visible-light 3D-3D  $\text{Bi}_2\text{WO}_6$ /graphene hydrogel (BWO/GH) photocatalyst with the synergistic effect of adsorption and photocatalysis has been successfully synthesized by a facile one-step hydrothermal method and is applied in environment remediation. 3D porous graphene hydrogel, in which 3D-structured flower-like BWO as an efficient photocatalyst is homogenously distributed, not only exhibits the great absorption toward the organic pollution, but also provides multidimensional quality and electron transfer channels. The 3D-3D structure of BWO/GH composite is beneficial to light refraction and reflection, which highly improves the utilization rate of light. The synergistic effect of the 3D-3D BWO/GH composite greatly enhanced the removal rates of organic pollutants and it is ease of separation and recycling in water purification. The removal rate of methylene blue (MB) by BWO/GH composite is about 2.3 times as that of the pure BWO in static systems, and the removal rates of MB and 2, 4-dichlorophenol (2, 4-CDP) are about 1.3 and 3 times as these of the pure BWO in dynamic system. When the irradiation time lasted for 74 h, the removal rate of MB is nearly unchanged and still kept at 36.1%, indicating that the 3D BWO/GH composite has a high stability. The construction of BWO/GH composite resolved the adsorption saturation problem of GH and improved the photocatalytic activity of BWO, thus greatly improved the removal rate of water pollutants.

© 2016 Elsevier B.V. All rights reserved.

## 1. Introduction

Environmental pollution problems have become increasingly serious with the rapid development of human society, especially the water pollution, which seriously affects our daily life [1–3]. It is well known that the adsorption method is one of the widely used strategies for the treatment of water pollution due to its advantages of low cost, high adsorption capacity, high adsorption rate and ease of operation [4–7]. Among diverse of adsorption materials, the 3D network structure of hydrogel [8–10], especially the 3D structural GH [11,12], has attracted much attention because it can reduce the aggregation and provide multidimensional mass transmission channel, and it is easy to separate from the mixture reaction solution. Compared with the traditional adsorption materials such as activated carbon [13,14], silica [15,16] and polymer resins [17], GH

shows much higher adsorption activity and adsorption rate for the organic compounds due to its high surface area, particular porous structure and the plane adsorption property, and it is widely used in the field of water pollution [18–21].

Although the absorption method is regarded as an effective method for water treatment, the hazardous water pollutants are just concentrated rather than mineralized to non-polluting substances by adsorption material. It might cause secondary pollution in waste water treatment. Furthermore, the adsorbents are generally difficult to regenerate and need to be treated to release the pollutant when reached their saturations [18,22]. Therefore, it is necessary to develop the new technology to remove the hazardous pollutants from water.

Photocatalysis has been widely used for waste water treatment because photocatalyst possesses excellent oxidation ability and it can decompose refractory organic pollutants and mineralize most toxic compounds completely [23–26]. However, some disadvantages such as the low visible-light absorption, high recombination efficiency of the photo-generated electron-hole pairs and

\* Corresponding authors.

E-mail addresses: [chendaimei@cugb.edu.cn](mailto:chendaimei@cugb.edu.cn) (D. Chen), [tzhangym@jnu.edu.cn](mailto:tzhangym@jnu.edu.cn) (Y. Zhang), [zhuyf@mail.tsinghua.edu.cn](mailto:zhuyf@mail.tsinghua.edu.cn) (Y. Zhu).

ease of agglomeration limit the photocatalysis for industrial application. Therefore, it is believed that the development of novel photocatalytic materials with the synergistic effect of pollutants adsorption-enrichment and photocatalytic degradation undoubtedly has the most significant for the water purification.

The combination of 3D structural hydrogel with photocatalyst to fabricate the 3D porous hydrogel-based composite photocatalyst can not only overcome the adsorption saturation and non-regeneration problems of adsorption material, but also can improve the adsorption property and the separation of powder photocatalysts [27,28]. In addition, photocatalyst can homogeneously distribute into the framework of 3D hydrogel, highly reducing the aggregation of powder photocatalyst and expose more active sites. It is beneficial to adsorption and surface photocatalytic reaction [29], thus effectively improves the removal rates of water pollutants. Compared with the other hydrogel-based photocatalyst, the GH-based photocatalyst has attracted much more attention in the field of water purification due to its special 3D porous structure, high surface area and good electrical conductivity [30]. The excellent electrical conductivity of GH can effectively promote the transfer of photo-generated electron, and the 3D porous structure can provide multidimensional quality and electron transfer channels, thus greatly enhance the photocatalytic performance. Until now, a few works about the 3D porous structural graphene aerogels (GA) based photocatalysts with high synergistic removal rates of water pollutants have been reported, such as 3D structural  $\text{TiO}_2$ /GA composite [31],  $\text{g-C}_3\text{N}_4$ /GA composite [32] and  $\text{AgX}/\text{GA}$  ( $\text{X} = \text{Br, Cl}$ ) composite [33]. However, the black graphene hydrogel can absorb the whole UV and visible light and greatly decrease the light absorption of the photocatalyst in porous GH. Therefore, improving the light absorption and utilization of the photocatalyst in GH-based composite is very important for the enhancement of photocatalytic efficiency. Compared to 2D, 1D and 0D photocatalysts, such as  $\text{g-C}_3\text{N}_4$  nanosheets and  $\text{TiO}_2$ , 3D hierarchical structural photocatalyst has higher light utilization efficiency due to the light refraction and reflection in the interior structure of photocatalyst. Therefore, the construction of the novel double three-dimensional (3D-3D) structural GH-based photocatalyst composite could greatly improve the light utilization efficiency and the photocatalytic performance of the photocatalyst.

Bi-based photocatalyst with high photocatalytic performance has attracted great interests [34–36].  $\text{Bi}_2\text{WO}_6$  (BWO), as an excellent visible-light-driven photocatalyst with a narrow band gap ( $\sim 2.8$  eV) [37], has a crystal structure composed of accumulated layers of alternating bismuth oxide ( $\text{Bi}_2\text{O}_2$ )<sup>2+</sup> layers and octahedral ( $\text{WO}_4$ )<sup>2-</sup> sheets [38,39]. The layered structure is favorable for electrons and holes transfer in different directions, which effectively inhibits the recombination of electrons and holes, thus leading to the high photocatalytic performance. It has caused extensive concern in the fields of energy conversion [26,40] and pollutants degradation [23,34,41,42] due to its unique molecular structure, reactivity, stability and high photocatalytic activity [43]. In our work, the 3D-3D porous structural BWO/GH composites were successfully synthesized by a facile one-step hydrothermal method. The efficient 3D flower-like BWO photocatalysts were settled in the 3D porous GH network and formed the 3D-3D porous structural BWO/GH composites. This particular structure of BWO/GH composite would improve the light utilization efficiency and absorption of the organic compound, and provide multidimensional quality and electron transfer channels. The photocatalytic performances of BWO/GH composites were evaluated by MB and 2, 4-CDP decomposing under visible light ( $\lambda \geq 420$  nm) in both static and dynamic systems. The 3D-3D structural BWO/GH composite may realize the synergistic effect of adsorption-enrichment and photocatalytic degradation. The GH-based photocatalyst composite resolves the

problem of adsorption saturation and regeneration, achieving a long term cycle utilization of adsorption material.

## 2. Experimental

### 2.1. Synthesis of BWO/GH composites

GO was prepared from graphite powder according to Hummer's method [44]. All other chemicals were of analytical grade and used without further purification. Deionized water was used throughout. In a typical synthesis method: BWO/GH was synthesized by a facile one-step hydrothermal method and then freeze-dried. Ethylene glycol was used to disperse  $\text{Bi}(\text{NO}_3)_3$  and control the morphology of BWO. In details, 0.5 mmol  $\text{Bi}(\text{NO}_3)_3 \cdot 5\text{H}_2\text{O}$  was dissolved into 10 mL ethylene glycol after ultrasound for 10 min, then 20 mL GO solution was added with stirring for another 10 min. Here,  $\text{Bi}(\text{NO}_3)_3$  can be dispersed evenly into GO solution. Then, 0.25 mmol  $\text{Na}_2\text{WO}_4 \cdot 2\text{H}_2\text{O}$  was added and the resultant suspension was stirred for 15 min. Subsequently, the suspension was put into a 50 mL Teflon vessel and then sealed in an autoclave and heated at 180 °C for 24 h. GO was reduced in the process of heating, and 3D porous structural GH was formed by  $\pi$ - $\pi$  stacking interactions and hydrogen bond interactions between GO nanosheets. The products were treated by freeze-drying after soaking 2–3 days in deionized water. A series of samples were synthesized by changing the molar quantities of  $\text{Bi}(\text{NO}_3)_3 \cdot 5\text{H}_2\text{O}$  and  $\text{Na}_2\text{WO}_4 \cdot 2\text{H}_2\text{O}$ , and keeping the volume of GO solution unchanged.

### 2.2. Characterizations

The as-prepared BWO/GH composites were analyzed by the thermogravimetry analysis (TG), the field emission gun scanning electron microscope (FE-SEM, Hitachi SU-8010) and the transmission electron microscopy (TEM, equip a Hitachi HT 7700 electron microscope) with an acceleration voltage of 100 kV. X-ray diffraction (XRD) patterns of BWO/GH samples were recorded by using a Bruker D8 Advance X-ray diffractometer ( $\text{Cu K}\alpha$ ,  $\lambda = 1.5406 \text{ \AA}$ , 40 kV, 40 mA). Fourier transfer infrared (FT-IR) spectra were performed by using a Bruker V70 spectrometer. Raman spectra were recorded on a microscopic confocal Raman spectrometer (HORIBA HR800, with an excitation of 514.5 nm laser light). The diffuse-reflectance spectrum (DRS) of BWO/GH composites were recorded on an UV-vis spectrophotometer (Hitachi, U-3010, equipped with an integrated sphere,  $\text{BaSO}_4$  used as the reference). The specific surface area and pore diameter distribution were measured by a Micromeritics ASAP2020 Surface Area and Porosity Analyzer.

### 2.3. Photocatalytic experiments

The adsorption and photocatalytic performances of different BWO/GH samples in static system were evaluated by degrading methylene blue (MB, 40 ppm) solution in a multi-tube agitated reactor (XPA-7) under visible-light irradiation ( $\lambda > 420$  nm). The visible light source was provided by a 500 W xenon lamp (filter,  $\lambda = 420$  nm). In the experiment, 25 mg photocatalyst was added into the prepared 50 mL MB solution (40 ppm). At given time intervals, 2.5 mL aliquots were sampled and centrifuged. The MB supernatant liquid was analyzed by recording variations of the maximum absorption peak (664 nm for MB) using a Hitachi U-3010 UV-vis spectrophotometer.

The synergistic effect of adsorption-enrichment and photocatalytic degradation of BWO/GH composites in dynamic system were evaluated by removing MB ( $1 \times 10^{-5}$  mol/L) and 2, 4-CDP (5 ppm) in solutions, which conducted in a homemade reactor with a quartz cover [27]. Peristaltic pump provided the power. Visible light source was provided by a xenon lamp (Perfectlight, filter,  $\lambda = 420$  nm).

100 mg photocatalyst was coated on the reactor with Ni mesh. The volume of the reactor is 65 mL. Turning on the peristaltic pump and light at the same time at the beginning of photocatalytic degradation reaction. At given time intervals, 3 mL aliquots were sampled. MB solutions were directly analyzed by recording variations of the maximum absorption peak (664 nm for MB) on a Hitachi U-3010 UV-vis spectrophotometer. 2, 4-CDP solutions were analyzed by recording variations of the 2, 4-CDP peak area on HPLC, which was used to detect the concentration of 2, 4-CDP.

#### 2.4. Electrochemical measurements

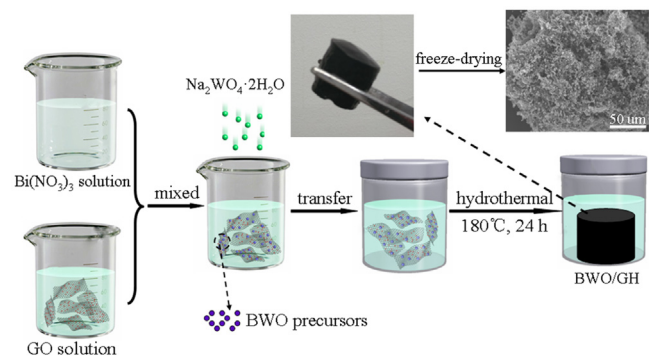
The photoelectrochemical properties of BWO/GH composites were measured on the three electrodes electrochemical system. The photoelectrochemical property of samples were performed on an electrochemical workstation (CHI-660D, China), with a conventional three-electrode cell. ITO deposited with photocatalyst served as a working electrode, a platinum wire and SCE served as the counter and reference electrode, respectively.  $\text{Na}_2\text{SO}_4$  solution (0.1 M) as the electrolyte solution. Mott–Schottky plots were generated with different frequency of 10, 100 and 1000 Hz.

### 3. Results and discussion

#### 3.1. Structure and morphology of BWO/GH composites

The one step synthesis of BWO/GH composite was illustrated in **Scheme 1**. The contents of BWO and GH in different samples were obtained by TG analysis. **Fig. 1** showed that the weight of BWO kept unchanged in the whole heating process, while both BWO/GH composites and GH had one large weight loss stage, which could attribute to the burning of GH. The weight losses of all BWO/GH composites and GH began at about 300 °C, and dramatically decreased within the temperature range from 500 °C to 560 °C. Based on the TG analysis, the real contents of BWO in 3D-structured BWO/GH composites were determined to be 78.31%, 85.39%, 89.89%, and 93.67%, respectively.

**Fig. 2** showed the FE-SEM images of morphology and microstructure of BWO, GH and BWO/GH composites. GH exhibited 3D porous network structure with interconnected pores composed by randomly oriented GO nanosheets (shown in **Fig. 2a**). And



**Scheme 1.** Schematic illustration of the synthetic process of 3D-BWO/GH composite.

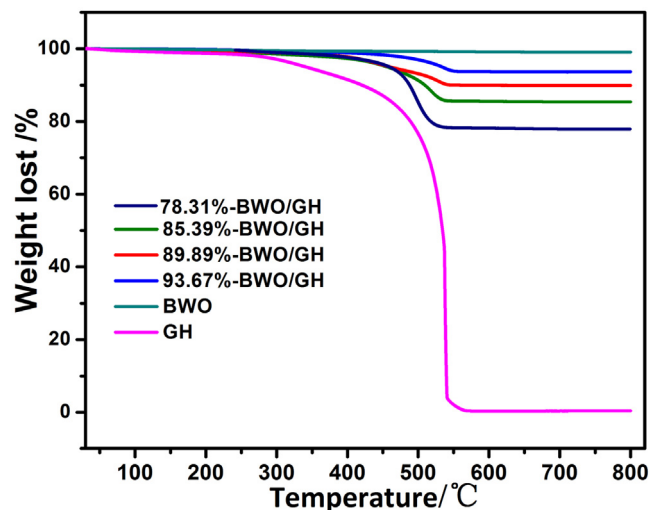


**Fig. 1.** Thermograms (TG) of GH, BWO and BWO/GH composites from 30 °C to 800 °C with a heating rate of 5 °C/min.

the three dimensional spatial reticulate structure of GH can be clearly observed by TEM (shown in **Fig. 3a**). **Fig. 2b** showed that the 3D flower-like BWO with diameters of about 3–5  $\mu\text{m}$  was con-

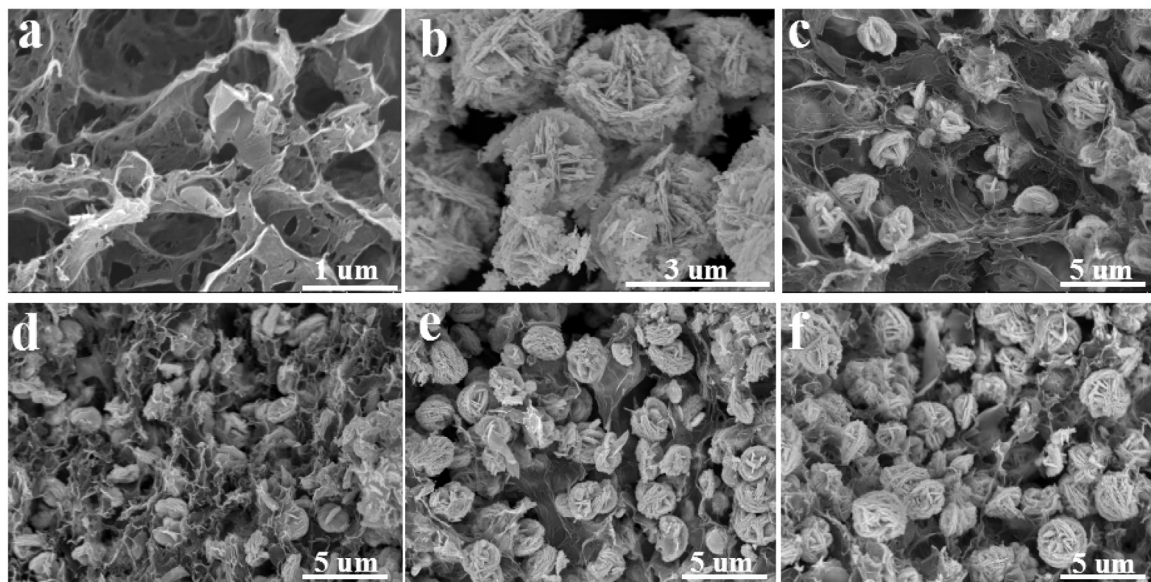


**Fig. 2.** FESEM images of a) BWO; b) GH; c) 78.31%-BWO/GH; d) 85.39%-BWO/GH; e) 89.89%-BWO/GH; and f) 93.67%-BWO/GH.

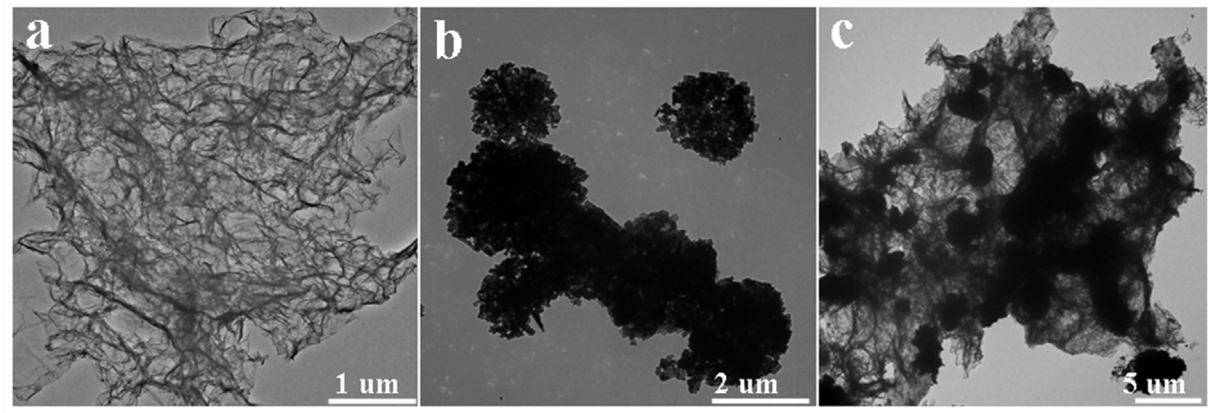


Fig. 3. The TEM pictures of a) GH; b) BWO; and c) 78.31%-BWO/GH composite.

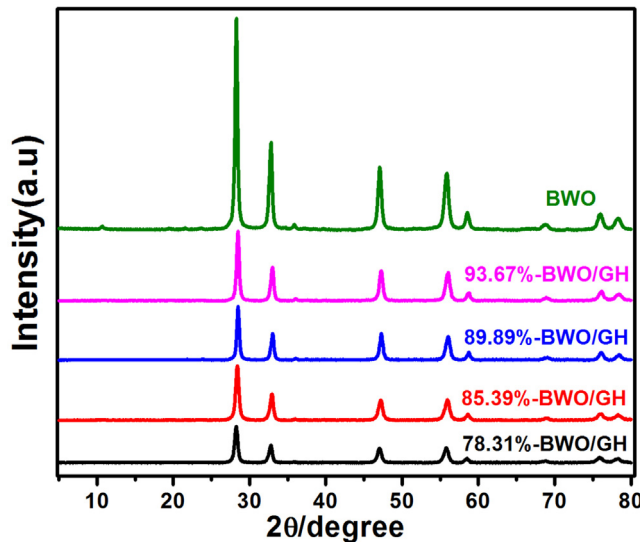


Fig. 4. XRD patterns of BWO and BWO/GH composites.

structed by BWO nanosheets with size of about 50–100 nm (Fig. S1). The TEM image of BWO (Fig. 3b) revealed the existence of BWO nanosheet accumulation pores, which is favorable to light refraction and reflection, resulting in the improvement of light utilization. The FE-SEM images of BWO/GH composites with different BWO contents were showed in Fig. 2c–f. The 3D flower-like BWO grew homogeneously into the framework of GH in composites. With the increases of BWO content, more and more flower-like BWO was exposed on the surface of the GH framework. Fig. 2c showed the morphology of 78.31%-BWO/GH composite, its internal structure could be further observed by TEM (shown in Fig. 3c), which further confirmed that the 3D flower-like BWO uniformly distributed into the 3D framework of GH. The EDS of 78.31%-BWO/GH composite and its corresponding EDS mappings were showed in Fig. S2, demonstrating that there were only C, Bi, O, and W elements in BWO/GH composite and they were evenly distributed. The FE-SEM and TEM characterizations indicated the successful preparation of the special 3D-3D structural BWO/GH composite photocatalyst.

Fig. 4 showed the XRD patterns of different BWO/GH composites. All the samples exhibited the distinctive peaks at  $2\theta = 28.3$ ,  $32.9$ ,  $33.6$ ,  $47.1$ ,  $55.9$ ,  $58.6$ , and  $68.8^\circ$ , which can be indexed to orthorhombic  $\text{Bi}_2\text{WO}_6$  (JCPDS: 16-0127, shown in Fig. S3). As the peak intensity of BWO was much higher than that of GH, the diffraction peaks of GH could not be observed obviously in BWO/GH composite. The peak intensity of BWO/GH composites decreased

with the increase of GH, indicating that the GH might inhibit the growth of BWO crystal to some extent but it did not affect the growth orientation of BWO.

The structure of BWO/GH composites can be further confirmed by Fourier transform infrared (FTIR) and Raman spectra. Fig. 5a showed the FTIR spectra of GH, BWO and BWO/GH composites. The FTIR spectra of the pure BWO and BWO/GH composites presented the main absorption peaks of BWO range from  $600$  to  $1000\text{ cm}^{-1}$ , which could be attributed to the stretching vibration of  $\text{Bi}=\text{O}$ ,  $\text{W}=\text{O}$  and  $\text{W}=\text{O}=\text{W}$  bridging stretching mode [45]. The main absorption peaks of GH could also be observed in all BWO/GH composites. The peaks of GH at  $1732\text{ cm}^{-1}$  and  $1574\text{ cm}^{-1}$  were assigned to  $\text{C}=\text{O}$  and  $\text{C}=\text{C}$  stretching vibration, and the peaks observed at  $1214\text{ cm}^{-1}$  and  $1015\text{ cm}^{-1}$  corresponded to  $\text{C}=\text{O}$  stretching and  $\text{C}=\text{O}=\text{C}$  bond [46]. The FTIR results indicated that the function groups and structures of GH and BWO had no changes in BWO/GH composite. Raman spectra of all samples were showed in Fig. 5b, as shown that all characteristic bands of the pure BWO and GH appeared in the Raman spectrum of BWO/GH composite. Both the GH and BWO/GH composites had two prominent peaks located at  $1344$  and  $1590\text{ cm}^{-1}$ , which assigned to the G band and D band of graphene. The integrated intensity ratio of  $I_D/I_G$  is used to characterize the degree of graphitization. As shown that the values of  $I_D/I_G < 1$  for GO, while the values of  $I_D/I_G > 1$  for all GH and BWO/GH composites, implying that GO was reduced into graphene during the hydrothermal process. Raman bands of BWO located at  $790$  and  $817\text{ cm}^{-1}$  are related to the symmetric and asymmetric  $\text{A}_g$  modes of terminal  $\text{O}=\text{W}=\text{O}$ , and the band located at  $707\text{ cm}^{-1}$  is related to the anti-symmetric bridging mode of the tungstate chain [47]. Meanwhile the bands located at  $256$ ,  $274$  and  $296\text{ cm}^{-1}$  are assigned to the bending of apical  $\text{O}=\text{W}=\text{O}$ , and the band located at  $406\text{ cm}^{-1}$  corresponds to the bending of equatorial  $\text{O}=\text{W}=\text{O}$ . The modes below  $150\text{ cm}^{-1}$  can be assigned to translations of the tungsten and bismuth ions [48]. Compared with the pure BWO, the intensity of inherent Raman bands of BWO in BWO/GH composites dramatically decreases with the increase of GH, and some bands become too weak to be observed obviously in the Raman spectra of BWO/GH. The Raman band of BWO at  $138\text{ cm}^{-1}$  moved to  $148\text{ cm}^{-1}$  with the increase of GH, suggesting there existed strong interaction between BWO and GH. Moreover, the Raman band at  $790\text{ cm}^{-1}$  and  $817\text{ cm}^{-1}$  became weaker with the increasing amount of GH and merged into one broad Raman band eventually. XRD shows that the existence of GH can affect the growth of BWO crystal and the little amount of amorphous  $\text{Bi}_2\text{WO}_6$  might occur in this BWO/GH composite [49]. The low crystallinity and a little amount of amorphous  $\text{Bi}_2\text{WO}_6$  result in weakening the Raman bands and merging the two Raman bands at  $790\text{ cm}^{-1}$  and  $817\text{ cm}^{-1}$  into one broad Raman band.

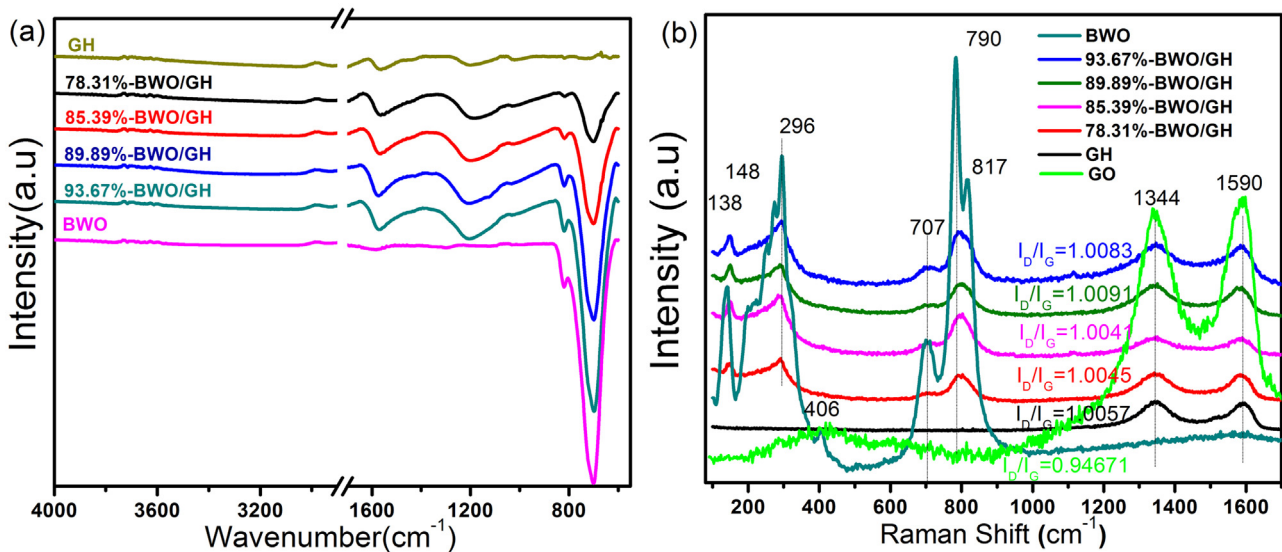


Fig. 5. a) FTIR spectra of GH, BWO and BWO/GH composites; b) Raman spectra of GH, BWO and BWO/GH composites.

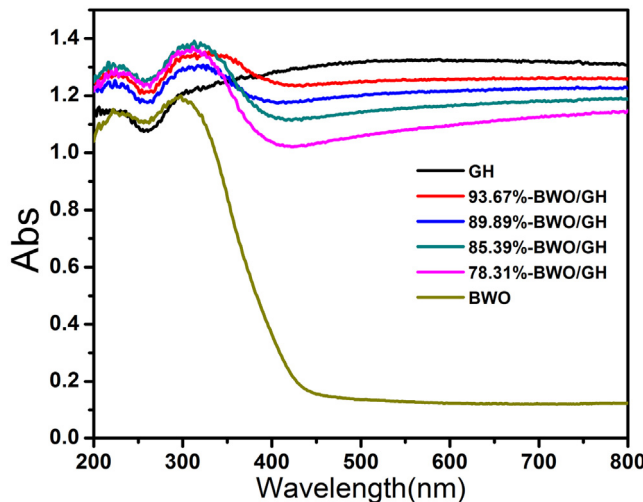


Fig. 6. UV-vis diffuse reflectance spectra (DRS) of GH, BWO and BWO/GH composites.

Fig. S4 exhibited the  $\text{N}_2$  adsorption-desorption isotherms and the corresponding pore-size distributions of BWO, GH and BWO/GH composites. Fig. S4a showed that BWO/GH composite possessed a typical mesoporous structure. The specific surface area of the pure BWO is only  $14.64 \text{ m}^2 \text{ g}^{-1}$ . Compared with the BWO, GH has a much higher specific surface area of  $278.16 \text{ m}^2 \text{ g}^{-1}$ . With the content of GH increasing from 7% to 22%, the specific surface areas of BWO/GH composites increase gradually from  $26.04 \text{ m}^2 \text{ g}^{-1}$  to  $35.24 \text{ m}^2 \text{ g}^{-1}$ , indicating GH can improve the surface area of the BWO/GH composite photocatalyst. According to Fig. S4b, it can be found that the pores of BWO/GH with pore diameter at about 10–40 nm, which is obviously much smaller than that of GH (20–60 nm). The smaller pore diameter may be attributed to the BWO nanosheet accumulation pores (shown in Fig. 3b) and the interaction between BWO and GH. BWO grown onto the surface of pores of GH, which has confirmed by SEM and TEM images previously, leading to a decrease of distribution range of pore diameter of GH.

The optical absorption properties of BWO, GH and BWO/GH composites were investigated by UV-vis diffuse reflectance spectroscopy (DRS). As shown in Fig. 6, the black GH exhibited a very strong absorption in the whole UV and visible light regions,

while the pure BWO had an inefficient visible light absorption with the light absorption edge at about 450 nm. The absorption edge of BWO/GH composite exhibited an apparent red shift as GH increased. Meanwhile, the absorption intensity of BWO/GH composite in visible light regions increased gradually with the increase of GH. As a result, the BWO/GH composite obtained a better ability of light harvest, which was beneficial to enhance the photocatalytic activity.

### 3.2. Photocatalytic performance in static system

Fig. 7a showed the adsorption properties of BWO/GH composites under the same experiment conditions in dark. It took about 2 h for BWO and all BWO/GH composites to get their adsorption desorption equilibriums in static system. The pure BWO could adsorb only about 3.1% of MB (initial concentration of 40 ppm), while GH could adsorb 92.7% of MB for 12 h. The adsorption proportion of MB by BWO/GH composite dramatically increased with the increase of GH, indicating that the presence of GH greatly enhanced the adsorption property of BWO/GH composite. The 78.31%-BWO/GH composite can adsorb about 26.7% of MB, which was about 8.6 times of the pure BWO. Photocatalytic degradation of MB by BWO/GH composite in static system was showed in Fig. 7b. Before light illumination, all mixed solutions of MB and photocatalyst kept stirring for 2 h in dark to reach their adsorption equilibriums. As can be seen, the removal rate of MB by the pure BWO was about 22.3% in 12 h and the BWO/GH composites greatly improved the removal rate which could be up to 50.6%. It was about 2.27 times of the pure BWO. The result confirmed that the introduction of GH not only greatly enhanced the adsorption of BWO/GH composites, but also greatly improved the photocatalytic performance of BWO/GH composites, achieving the synergistic effect of adsorption-enrichment and photocatalytic degradation.

### 3.3. Photocatalytic performance in dynamic system

In order to further investigate the synergistic effect of BWO/GH composite, long-time detections of MB and 2, 4-CDP solutions in dynamic system were designed. Fig. 8a showed the synergistic removal of MB by adsorption and photocatalysis over 78.31%-BWO/GH composite with different flow rates in dynamic system. The result indicated that the flow rate obviously affected the removal rate of pollutant and equilibrium time of BWO/GH com-

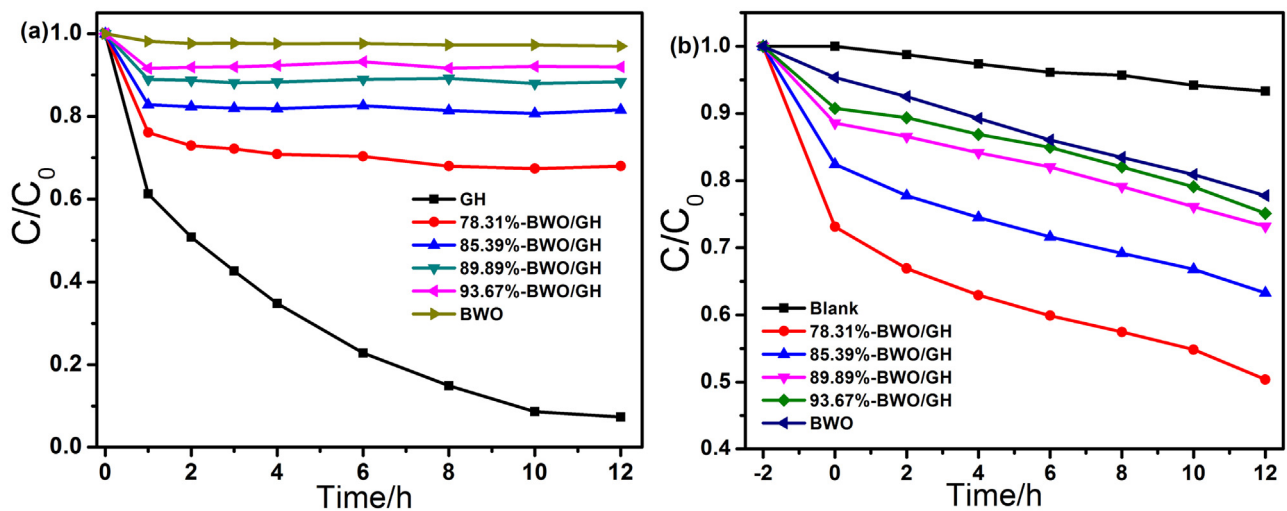


**Fig. 7.** a) Adsorption of MB by BWO, GH and BWO/GH composites in static system. b) The synergistic removal of MB by BWO and BWO/GH composites under visible-light irradiation ( $\lambda > 420$  nm) in static system.

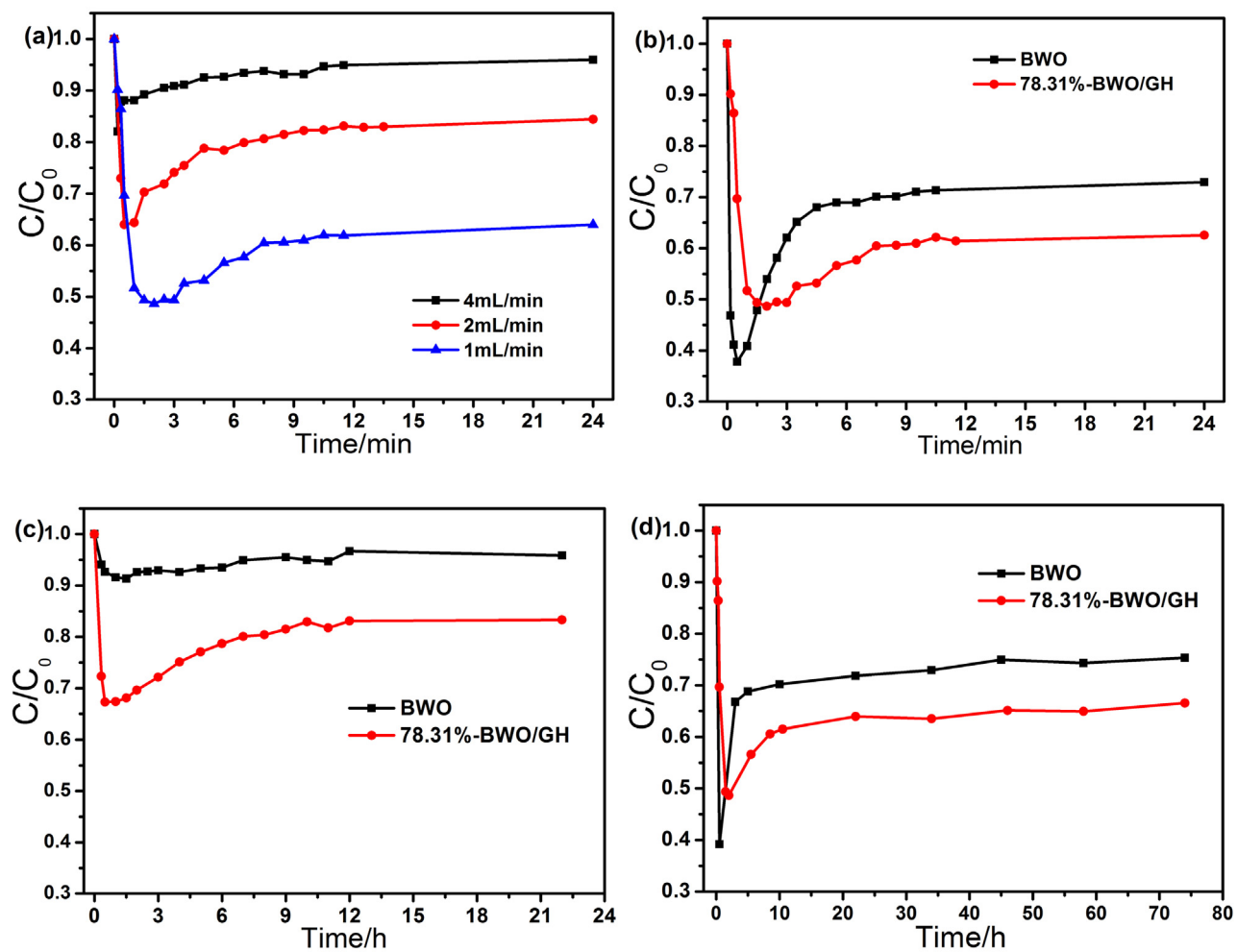


**Fig. 8.** a) Adsorption and photocatalysis synergistic removal of MB over 78.31%-BWO/GH composite with different flow rates in dynamic system; b and c) Adsorption and photocatalytic degradation synergistic removal of MB and 2, 4-CDP by BWO and 78.31%-BWO/GH composite with 1 mL/min flow rate in dynamic system; d) Photocatalytic stability experiment of BWO and 78.31%-BWO/GH composite with 1 mL/min flow rate.

posite. As the flow rate decreased, the removal rate of MB increased and the time for adsorption-desorption equilibrium became longer. Fig. S5 showed the adsorption properties of different BWO/GH

composites in dynamic system with the flow rate at 1 mL/min. The concentrations ( $C$ ) of MB solutions that flowed over the reactor nearly came back to  $C_0$  ( $1 \times 10^{-5}$  mol/L) when the BWO/GH

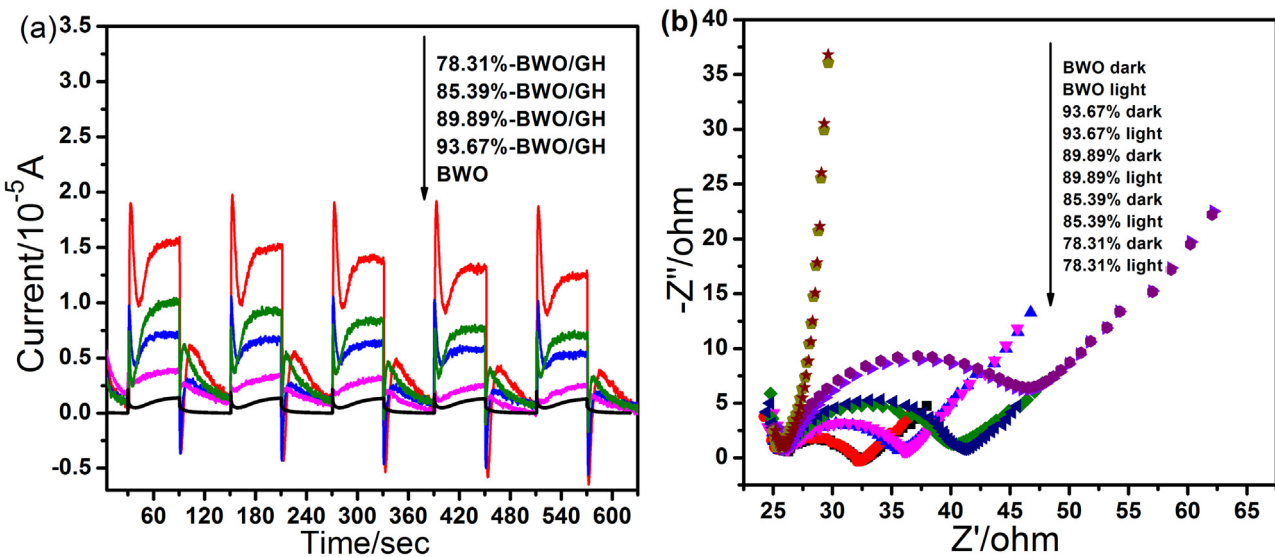


**Fig. 9.** a) Transient photocurrent responses of BWO and BWO/GH composites; b) and the corresponding electrochemical impedance spectroscopy (EIS) Nyquist plots of samples.

composites got adsorption-desorption equilibriums. All BWO/GH composites and BWO could attain their adsorption-desorption equilibriums in 8 h and the equilibrium time increased with the increase of GH. Fig. 8 showed the synergistic removal rates of MB and 2, 4-CDP over the pure BWO and 78.31%-BWO/GH composite with 1 mL/min flow rate. As shown in Fig. 8b, it took about 4 h for BWO to reach adsorption-desorption equilibrium and the removal rate of MB kept at about 28.1%. While the time to reach adsorption-desorption equilibrium for 78.31%-BWO/GH composite was about 8 h and the removal rate of MB kept at about 38.5%. Fig. 8c showed the synergy effect of adsorption and photocatalytic degradation of 2, 4-CDP by 78.31%-BWO/GH composite and BWO in dynamic system with flow rate at 1 mL/min. As shown that, the pure BWO hardly had any ability to remove 2, 4-CDP in solution, however, the 78.31%-BWO/GH exhibited an obvious removal ability for 2, 4-CDP. It took about 8 h for 78.31%-BWO/GH to attain adsorption-desorption equilibrium and then kept a stable degradation rate at about 17%, which was about 3 times higher than that of the pure BWO. The results further confirmed that the photocatalytic performance of BWO/GH composite was greatly enhanced and the BWO/GH composite achieved the synergistic effect of adsorption and photocatalytic degradation, thus greatly improved the removal rates of organic pollutants.

In order to evaluate the stability of BWO/GH composite, the stability experiment was also conducted in dynamic system with 1 mL/min flow rate. Fig. 8d showed the photostability results of the BWO and 78.31%-BWO/GH composite. As shown that, when the BWO and 78.31%-BWO/GH composite reached their adsorption-desorption equilibriums, the removal rates of MB were about 29.7% and 38.5%. Both the pure BWO and the 78.31%-BWO/GH composite kept very stable removal rates of MB. When the irradiation time reached 74 h, the removal rate of MB by the pure BWO was kept at 25.2% and the removal rate of MB over the 78.31%-BWO/GH composite was still 36.1%. The result demonstrated that the BWO/GH composite was very stable. Fig. S6 showed the morphology and microstructure comparisons of 78.31%-BWO/GH composite before and after the photostability experiment. It can be obviously observed that the morphology and microstructure of 78.31%-BWO/GH composite almost had no changes before and after the photostability experiment, indicating that BWO/GH composite had a very stable 3D-3D structure. The high stability of the

microstructure of BWO/GH composite is a prerequisite to ensure the stability of its photocatalytic performance.

### 3.4. Mechanism of photocatalytic activity enhancement

The enhanced photocatalytic performance of BWO/GH composite was further explored by photoelectrochemistry. Fig. 9 showed the transient photocurrent responses of BWO and BWO/GH composites and their corresponding electrochemical impedance spectroscopy (EIS) Nyquist plots. As shown in Fig. 9a, the transient photocurrent responses of all samples are very stable in cycles. The pure BWO had a very weak photocurrent response under the intermittent irradiation of visible light ( $\lambda > 420$  nm), which was only  $2.2 \times 10^{-6}$  A. Compared with the pure BWO, the transient photocurrent response of BWO/GH composite dramatically increased with the increase of GH. The 78.31%-BWO/GH composite had the highest photocurrent response ( $1.58 \times 10^{-5}$  A), which was 7.2 times of the pure BWO. The increased photocurrent response indicated that the separation efficiency of photoinduced carries were greatly enhanced, which was beneficial to enhance photocatalytic performance. Fig. 9b showed the corresponding typical electrochemical impedance spectroscopy (EIS) Nyquist plots of samples. The arc radiiuses of all BWO/GH composites and BWO under visible light irradiation were much smaller than those without light irradiation, indicating that BWO/GH composites and BWO could be excited under visible light ( $\lambda > 420$  nm). The arc radius of BWO/GH composites decreased with the increase of GH, demonstrating that the charge transfer resistance and the solid state interface layer resistance decreased dramatically with the increase of GH. The EIS confirmed that there was a tight connection between the interfaces of BWO and GH, through which charges could rapidly transfer and diffuse toward multi-directions. This means that the introduction of GH facilitated the separation and transfer of photoinduced electrons and holes. PL spectra further confirmed the suppression of the recombination of photo-generated electron-hole pairs (Fig. S7). All these results mentioned above demonstrated that the separation and transfer efficiency of photoinduced carries were greatly enhanced by the introduction of GH in composite. Consequently, BWO/GH composite would achieve a higher photocatalytic performance.

In order to further reveal the specific active species of BWO/GH composite in photocatalytic degradation reaction, the trapping

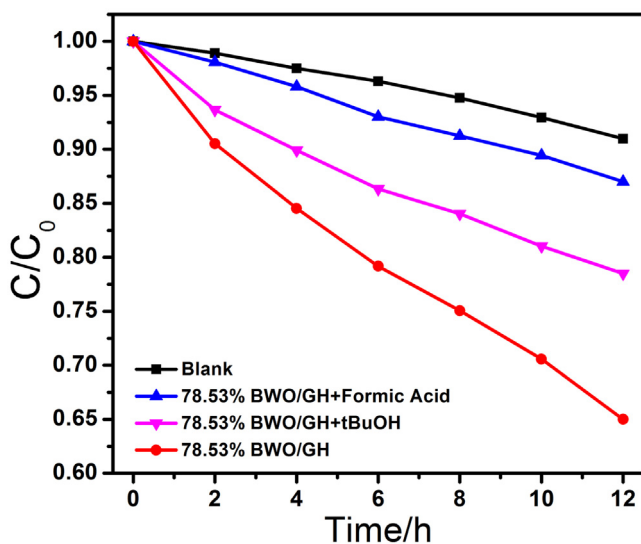


**Fig. 10.** The active species trapping by degrading MB over 78.31% BWO/GH composite in the static system.

experiment and electron spin resonance (ESR) measurement were conducted. Fig. 10 showed the result of the trapping experiments by using formic acid and *t*-BuOH as holes ( $h^+$ ) scavenger [50] and hydroxyl radical ( $\cdot OH$ ) scavenger [51], respectively. As shown in Fig. 10, the photocatalytic performance of 78.31%-BWO/GH decreased dramatically with adding hole scavenger (formic acid) and slightly decreased with adding  $\cdot OH$  scavenger (*t*-BuOH). At the same time, a strong signal response of  $\cdot OH$  was checked by ESR spectrum (shown in Fig. 11a), and there was no signal response for superoxide radical (shown in Fig. 11b). The ESR spectra further indicated that  $\cdot OH$  might be responsible for the photocatalytic degradation and  $O_2^-$  wasn't the active specie. The ESR and the trapping experiments confirmed that  $h^+$  was the main active specie in photocatalytic degradation of organic compounds, and  $\cdot OH$  also had the effect on the photocatalytic degradation to some extent.

From the Mott-Schottky (MS) plots and the plot of  $(\alpha h\nu)^{1/2}$  versus  $h\nu$  in Fig. S8, the calculated conduction band edge of as-prepared BWO is about 0.15 eV, and the band gap is around

2.81 eV. So the calculated valence band edge of BWO is around 2.96 eV, and the band structure of BWO/GH was showed in Fig. S9. Based on all above analysis, a mechanism of the synergy of pollutants adsorption-enrichment and photocatalytic degradation by BWO/GH composite was proposed (Fig. 12). In the synergistic process, the 3D GH worked as the supporter for BWO photocatalyst and it could adsorb and enrich the organic pollutants onto the surface of BWO/GH composite rapidly. As the adsorption-enrichment and photocatalytic degradation of pollutants occurred at the adjacent sites, the rapid enrichment of pollutant molecules reduced their diffusion distances, which was beneficial to accelerate the photocatalytic rate. BWO was excited and generated photo-generated electrons and holes when irradiated under the visible light. The holes on the valence band (VB) of BWO partly reacted with  $H_2O$  and generated  $\cdot OH$  radical [37]. Both the holes and  $\cdot OH$  radicals have deep oxidation ability, which can oxidize the organic pollutants into  $H_2O$  and  $CO_2$  completely. The electrons that on the conduction band (CB) of BWO rapidly transferred to the 3D structural GH thanks to the excellent conductivity of GH, highly improved the separation efficiency of photo-generated electrons and holes and enhanced the photocatalytic performance. The 3D network structural BWO/GH composite photocatalyst with the synergistic effect of adsorption-enrichment and photocatalytic degradation is easy to separate and recycle, and it achieves the long term utilization in dynamic system.

#### 4. Conclusions

In conclusion, we successfully synthesized 3D-3D BWO/GH composites by a facile one-step hydrothermal method. The 3D porous GH network setting with the efficient 3D flower-like BWO photocatalyst not only has the great absorption ability toward the organic compounds, but also provides multidimensional quality and electron transfer channels. The 3D-3D BWO/GH composite is easy to separate and recycle, exhibiting higher removal rates of MB and 2, 4-CDP in water purification due to the synergistic effect of adsorption-enrichment and photocatalysis. The removal rate of MB over 78.31%-BWO/GH composite was about 2.27 times as high as that of the pure BWO in static system, and the removal rates of MB and 2, 4-CDP were about 1.37 times and 3 times higher than those of the pure BWO in dynamic system. BWO/GH composite

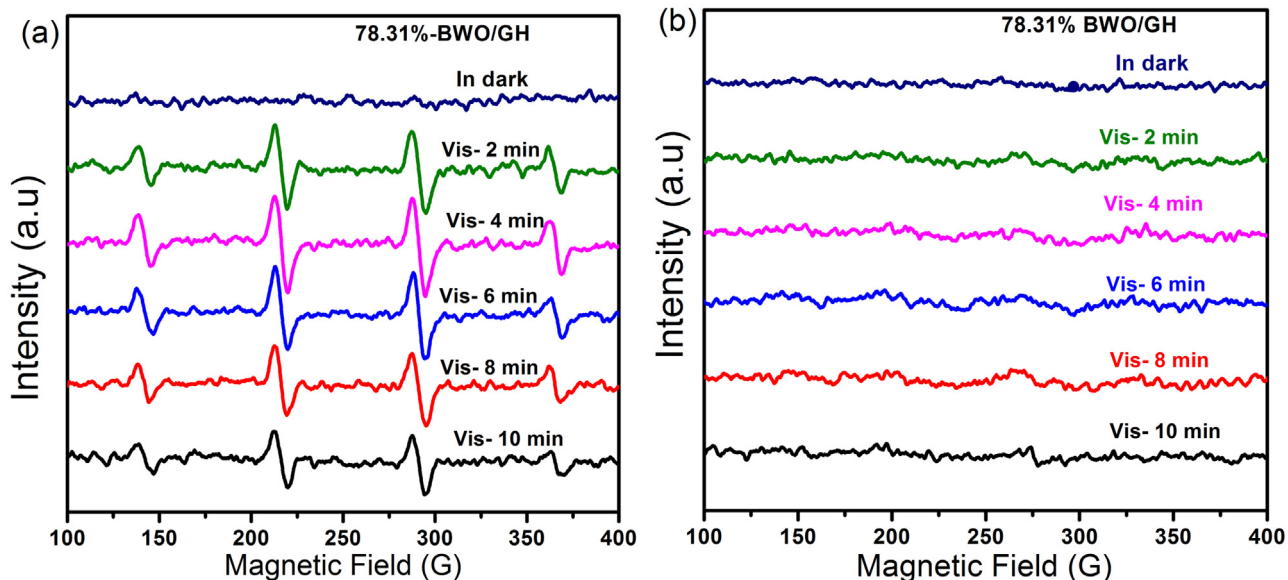


**Fig. 11.** Electron spin resonance (ESR) spectra of radical adducts trapped by DMPO; (a) DMPO- $\cdot OH$  radical species detected for the sample dispersion in water; (b) DMPO- $O_2^-$  radical species detected for the sample dispersion in methanol.

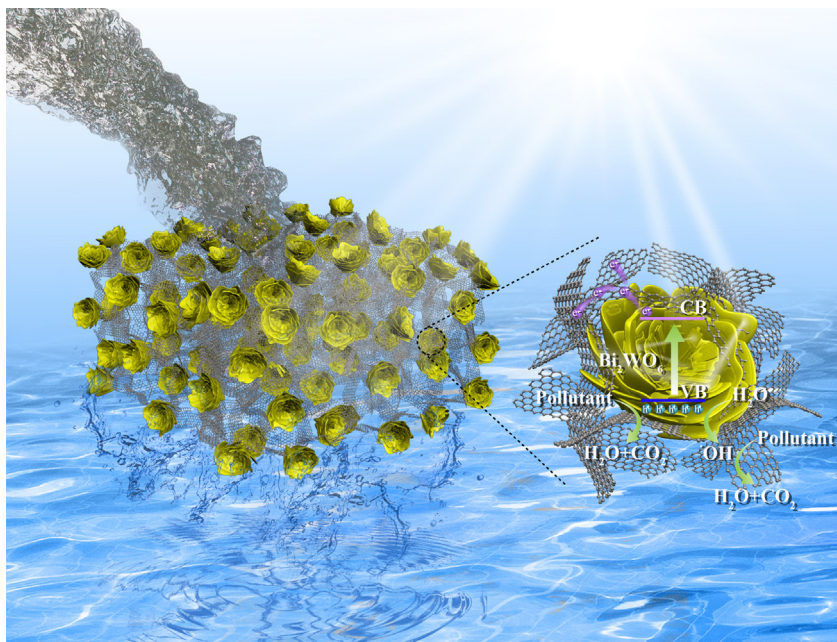


**Fig. 12.** Schematic drawing illustrates the synergy of pollutants adsorption-enrichment and photocatalytic degradation by BWO/GH composite.

exhibited a high stability and could be utilized for a long time. The BWO/GH composite with the synergistic effect of adsorption-enrichment and photocatalytic degradation would be a promising strategy for practical water pollutants treatment.

## Acknowledgements

This work was partly supported by the National Natural Science Foundations of China (Grant No. 21577132), the Fundamental Research Funds for the Central Universities (Grant No. 2652015225).

## Appendix A. Supplementary data

Supplementary data associated with this article can be found, in the online version, at <http://dx.doi.org/10.1016/j.apcatb.2016.12.035>.

## References

- M.A. Shannon, P.W. Bohn, M. Elimelech, J.G. Georgiadis, B.J. Mariñas, A.M. Mayes, Science and technology for water purification in the coming decades, *Nature* 452 (2008) 301–310.
- M.A. Montgomery, M. Elimelech, Water and sanitation in developing countries: including health in the equation, *Environ. Sci. Technol.* 41 (2007) 17–24.
- F. He, W. Wang, J.-W. Moon, J. Howe, E.M. Pierce, L. Liang, Rapid removal of Hg (II) from aqueous solutions using thiol-functionalized Zn-doped biomagnetite particles, *ACS Appl. Mater. Inter.* 4 (2012) 4373–4379.
- Z. Geng, Y. Lin, X. Yu, Q. Shen, L. Ma, Z. Li, N. Pan, X. Wang, Highly efficient dye adsorption and removal: a functional hybrid of reduced graphene oxide- $\text{Fe}_3\text{O}_4$  nanoparticles as an easily regenerative adsorbent, *J. Mater. Chem.* 22 (2012) 3527–3535.
- J. Fan, Z. Shi, M. Lian, H. Li, J. Yin, Mechanically strong graphene oxide/sodium alginate/polyacrylamide nanocomposite hydrogel with improved dye adsorption capacity, *J. Mater. Chem. A* 1 (2013) 7433–7443.
- I.E.M. Carpio, J.D. Mangadlao, H.N. Nguyen, R.C. Advincula, D.F. Rodrigues, Graphene oxide functionalized with ethylenediamine triacetic acid for heavy metal adsorption and anti-microbial applications, *Carbon* 77 (2014) 289–301.
- J. Ren, H.A. Abbood, F. He, H. Peng, K. Huang, Magnetic EDTA-modified chitosan/SiO<sub>2</sub>/Fe<sub>3</sub>O<sub>4</sub> adsorbent: preparation, characterization, and application in heavy metal adsorption, *Chem. Eng. J.* 226 (2013) 300–311.
- N. Li, R. Bai, A novel amine-shielded surface cross-linking of chitosan hydrogel beads for enhanced metal adsorption performance, *Ind. Eng. Chem. Res.* 44 (2005) 6692–6700.
- S. Deng, H. Xu, X. Jiang, J. Yin, Poly (vinyl alcohol)(PVA)-enhanced hybrid hydrogels of hyperbranched poly (ether amine)(hPEA) for selective adsorption and separation of dyes, *Macromolecules* 46 (2013) 2399–2406.
- J.L. Gurav, I.-K. Jung, H.-H. Park, E.S. Kang, D.Y. Nadargi, Silica aerogel: synthesis and applications, *J. Nanomater.* 2010 (2010) 23.
- J.N. Tiwari, K. Mahesh, N.H. Le, K.C. Kemp, R. Timilsina, R.N. Tiwari, K.S. Kim, Reduced graphene oxide-based hydrogels for the efficient capture of dye pollutants from aqueous solutions, *Carbon* 56 (2013) 173–182.
- Y. Chen, L. Chen, H. Bai, L. Li, Graphene oxide-chitosan composite hydrogels as broad-spectrum adsorbents for water purification, *J. Mater. Chem. A* 1 (2013) 1992–2001.
- G. Mezohegyi, F.P. van der Zee, J. Font, A. Fortuny, A. Fabregat, Towards advanced aqueous dye removal processes: a short review on the versatile role of activated carbon, *J. Environ. Manage.* 102 (2012) 148–164.
- F. Nekouei, S. Nekouei, I. Tyagi, V.K. Gupta, Kinetic, thermodynamic and isotherm studies for acid blue 129 removal from liquids using copper oxide nanoparticle-modified activated carbon as a novel adsorbent, *J. Mol. Liq.* 201 (2015) 124–133.
- E. Repo, J.K. Warchoł, A. Bhatnagar, M. Sillanpää, Heavy metals adsorption by novel EDTA-modified chitosan–silica hybrid materials, *J. Colloid Interface Sci.* 358 (2011) 261–267.
- J. Roosen, J. Spooren, K. Binnemans, Adsorption performance of functionalized chitosan–silica hybrid materials toward rare earths, *J. Mater. Chem. A* 2 (2014) 19415–19426.
- Y. Zhang, Y. Li, L.-q. Yang, X.-j. Ma, L.-y. Wang, Z.-F. Ye, Characterization and adsorption mechanism of Zn<sup>2+</sup> removal by PVA/EDTA resin in polluted water, *J. Hazard. Mater.* 178 (2010) 1046–1054.
- R. Xu, G. Zhou, Y. Tang, L. Chu, C. Liu, Z. Zeng, S. Luo, New double network hydrogel adsorbent: highly efficient removal of Cd (II) and Mn (II) ions in aqueous solution, *Chem. Eng. J.* 275 (2015) 179–188.
- H. Gao, Y. Sun, J. Zhou, R. Xu, H. Duan, Mussel-inspired synthesis of polydopamine-functionalized graphene hydrogel as reusable adsorbents for water purification, *ACS Appl. Mater. Interfaces* 5 (2013) 425–432.
- Z.Y. Sui, Y. Cui, J.H. Zhu, B.H. Han, Preparation of three-dimensional graphene oxide-polyethylenimine porous materials as dye and gas adsorbents, *ACS Appl. Mater. Inter.* 5 (2013) 9172–9179.
- J. Xu, L. Wang, Y. Zhu, Decontamination of bisphenol A from aqueous solution by graphene adsorption, *Langmuir* 28 (2012) 8418–8425.
- X. Mi, G. Huang, W. Xie, W. Wang, Y. Liu, J. Gao, Preparation of graphene oxide aerogel and its adsorption for Cu<sup>2+</sup> ions, *Carbon* 50 (2012) 4856–4864.
- M. Qamar, R.B. Elsayed, K.R. Alhooshani, M.I. Ahmed, D.W. Bahneemann, Highly efficient and selective oxidation of aromatic alcohols photocatalyzed by nanoporous hierarchical Pt/Bi<sub>2</sub>WO<sub>6</sub> in organic solvent-free environment, *ACS Appl. Mater. Interfaces* 7 (2015) 1257–1269.
- J. Yang, X. Wang, X. Zhao, J. Dai, S. Mo, Synthesis of uniform Bi<sub>2</sub>WO<sub>6</sub>-Reduced graphene oxide nanocomposites with significantly enhanced photocatalytic reduction activity, *J. Phys. Chem. C* 119 (2015) 3068–3078.
- W. Liu, J. Cai, Z. Ding, Z. Li, TiO<sub>2</sub>/RGO composite aerogels with controllable and continuously tunable surface wettability for varied aqueous photocatalysis, *Appl. Catal. B: Environ.* 174–175 (2015) 421–426.

[26] M. Li, L. Zhang, X. Fan, Y. Zhou, M. Wu, J. Shi, Highly selective  $\text{CO}_2$  photoreduction to CO over g-C<sub>3</sub>N<sub>4</sub>/Bi<sub>2</sub>WO<sub>6</sub> composites under visible light, *J. Mater. Chem. A* 3 (2015) 5189–5196.

[27] W. Jiang, Y. Liu, J. Wang, M. Zhang, W. Luo, Y. Zhu, Separation-free polyaniline/TiO<sub>2</sub> 3D hydrogel with high photocatalytic activity, *Adv. Mater. Interfaces* 3 (2016).

[28] M. Zhang, W. Jiang, D. Liu, J. Wang, Y. Liu, Y. Zhu, Y. Zhu, Photodegradation of phenol via C<sub>3</sub>N<sub>4</sub>-agar hybrid hydrogel 3D photocatalysts with free separation, *Appl. Catal. B: Environ.* 183 (2016) 263–268.

[29] J. Zhang, M. Zhang, C. Yang, X. Wang, Nanospherical carbon nitride frameworks with sharp edges accelerating charge collection and separation at a soft photocatalytic interface, *Adv. Mater.* 26 (2014) 4121–4126.

[30] H. Hu, Z. Zhao, W. Wan, Y. Gogotsi, J. Qiu, Ultralight and highly compressible graphene aerogels, *Adv. Mater.* 25 (2013) 2219–2223.

[31] B. Qiu, M. Xing, J. Zhang, Mesoporous TiO<sub>2</sub> nanocrystals grown in situ on graphene aerogels for high photocatalysis and lithium-ion batteries, *J. Am. Chem. Soc.* 136 (2014) 5852–5855.

[32] Z. Tong, D. Yang, J. Shi, Y. Nan, Y. Sun, Z. Jiang, Three-Dimensional porous aerogel constructed by g-C<sub>3</sub>N<sub>4</sub> and graphene oxide nanosheets with excellent visible-light photocatalytic performance, *ACS Appl. Mater. Interfaces* 7 (2015) 25693–25701.

[33] Y. Fan, W. Ma, D. Han, S. Gan, X. Dong, L. Niu, Convenient recycling of 3D AgX/graphene aerogels (X = Br, Cl) for efficient photocatalytic degradation of water pollutants, *Adv. Mater.* 27 (2015) 3767–3773.

[34] H. Huang, Y. He, Z. Lin, L. Kang, Y. Zhang, Two novel Bi-Based borate photocatalysts: crystal structure, electronic structure, photoelectrochemical properties, and photocatalytic activity under simulated solar light irradiation, *J. Phys. Chem. C* 117 (2013) 22986–22994.

[35] H. Huang, K. Xiao, Y. He, T. Zhang, F. Dong, X. Du, Y. Zhang, In situ assembly of BiOI@Bi<sub>12</sub>O<sub>17</sub>C<sub>2</sub> p-n junction: charge induced unique front-lateral surfaces coupling heterostructure with high exposure of BiOI {001} active facets for robust and nonselective photocatalysis, *Appl. Catal. B: Environ.* 199 (2016) 75–86.

[36] H. Huang, X. Li, J. Wang, F. Dong, P.K. Chu, T. Zhang, Y. Zhang, Anionic group self-doping as a promising strategy: band-gap engineering and multi-functional applications of high-performance  $\text{CO}_3^{2-}$ -doped Bi<sub>2</sub>O<sub>2</sub>CO<sub>3</sub>, *ACS Catal.* 5 (2015) 4094–4103.

[37] J. Sheng, X. Li, Y. Xu, Generation of H<sub>2</sub>O<sub>2</sub> and OH radicals on Bi<sub>2</sub>WO<sub>6</sub> for phenol degradation under visible light, *ACS Catal.* 4 (2014) 732–737.

[38] C. Li, G. Chen, J. Sun, H. Dong, Y. Wang, C. Lv, Construction of Bi<sub>2</sub>WO<sub>6</sub> homojunction via QDs self-decoration and its improved separation efficiency of charge carriers and photocatalytic ability, *Appl. Catal. B: Environ.* 160 (2014) 383–389.

[39] J. Tian, Y. Sang, G. Yu, H. Jiang, X. Mu, H. Liu, A Bi<sub>2</sub>WO<sub>6</sub>-based hybrid photocatalyst with broad spectrum photocatalytic properties under UV-vis, and near-infrared irradiation, *Adv. Mater.* 25 (2013) 5075–5080.

[40] Y. Zhou, Z. Tian, Z. Zhao, Q. Liu, J. Kou, X. Chen, J. Gao, S. Yan, Z. Zou, High-yield synthesis of ultrathin and uniform Bi<sub>2</sub>WO<sub>6</sub> square nanoplates benefiting from photocatalytic reduction of CO<sub>2</sub> into renewable hydrocarbon fuel under visible light, *ACS Appl. Mater. Inter.* 3 (2011) 3594–3601.

[41] Y. Chen, J. Fang, S. Lu, W. Xu, Z. Liu, X. Xu, Z. Fang, One-step hydrothermal synthesis of BiOI/Bi<sub>2</sub>WO<sub>6</sub> hierarchical heterostructure with highly photocatalytic activity, *J. Chem. Technol. Biotechnol.* 90 (2015) 947–954.

[42] D. He, L. Wang, D. Xu, J. Zhai, D. Wang, T. Xie, Investigation of photocatalytic activities over Bi<sub>2</sub>WO<sub>6</sub>/ZnWO<sub>4</sub> composite under UV light and its photoinduced charge transfer properties, *ACS Appl. Mater. Interfaces* 3 (2011) 3167–3171.

[43] L. Wu, J. Bi, Z. Li, X. Wang, X. Fu, Rapid preparation of Bi<sub>2</sub>WO<sub>6</sub> photocatalyst with nanosheet morphology via microwave-assisted solvothermal synthesis, *Catal. Today* 131 (2008) 15–20.

[44] W.S. Hummers Jr., R.E. Offeman, Preparation of graphitic oxide, *J. Am. Chem. Soc.* 80 (1958) 1339.

[45] J. Yu, J. Xiong, B. Cheng, Y. Yu, J. Wang, Hydrothermal preparation and visible-light photocatalytic activity of Bi<sub>2</sub>WO<sub>6</sub> powders, *J. Solid State Chem.* 178 (2005) 1968–1972.

[46] Z. Han, Z. Tang, P. Li, G. Yang, Q. Zheng, J. Yang, Ammonia solution strengthened three-dimensional macro-porous graphene aerogel, *Nanoscale* 5 (2013) 5462–5467.

[47] H. Fu, L. Zhang, W. Yao, Y. Zhu, Photocatalytic properties of nanosized Bi<sub>2</sub>WO<sub>6</sub> catalysts synthesized via a hydrothermal process, *Appl. Catal. B: Environ.* 66 (2006) 100–110.

[48] M. Mączka, A.F. Fuentes, L. Kępiński, M.R. Diaz-Guillen, J. Hanuza, Synthesis and electrical, optical and phonon properties of nanosized Aurivillius phase Bi<sub>2</sub>WO<sub>6</sub>, *Mater. Chem. Phys.* 120 (2010) 289–295.

[49] M. Mączka, L. Macalik, K. Hermanowicz, L. Kępiński, P. Tomaszewski, Phonon properties of nanosized bismuth layered ferroelectric material-Bi<sub>2</sub>WO<sub>6</sub>, *J. Raman Spectrosc.* 41 (2010) 1059–1066.

[50] T. Tan, D. Beydoun, R. Amal, Effects of organic hole scavengers on the photocatalytic reduction of selenium anions, *J. Photochem. Photobiol. A* 159 (2003) 273–280.

[51] H. Lee, W. Choi, Photocatalytic oxidation of arsenite in TiO<sub>2</sub> suspension: kinetics and mechanisms, *Environ. Sci. Technol.* 36 (2002) 3872–3878.